

THE STORAGE AND DISSIPATION OF MAGNETIC ENERGY IN THE QUIET SUN CORONA DETERMINED FROM *SDO*/HMI MAGNETOGRAMS

K. A. MEYER¹, J. SABOL¹, D. H. MACKAY¹, AND A. A. VAN BALLEGOOIJEN²

¹ School of Mathematics and Statistics, University of St Andrews, North Haugh, St Andrews KY16 9SS, UK; karen@mcs.st-and.ac.uk

² Harvard-Smithsonian Center for Astrophysics, 60 Garden Street, Cambridge, MA 02138, USA

Received 2013 January 31; accepted 2013 May 1; published 2013 May 30

ABSTRACT

In recent years, higher cadence, higher resolution observations have revealed the quiet-Sun photosphere to be complex and rapidly evolving. Since magnetic fields anchored in the photosphere extend up into the solar corona, it is expected that the small-scale coronal magnetic field exhibits similar complexity. For the first time, the quiet-Sun coronal magnetic field is continuously evolved through a series of non-potential, quasi-static equilibria, deduced from magnetograms observed by the Helioseismic and Magnetic Imager on board the *Solar Dynamics Observatory*, where the photospheric boundary condition which drives the coronal evolution exactly reproduces the observed magnetograms. The build-up, storage, and dissipation of magnetic energy within the simulations is studied. We find that the free magnetic energy built up and stored within the field is sufficient to explain small-scale, impulsive events such as nanoflares. On comparing with coronal images of the same region, the energy storage and dissipation visually reproduces many of the observed features. The results indicate that the complex small-scale magnetic evolution of a large number of magnetic features is a key element in explaining the nature of the solar corona.

Key words: Sun: corona – Sun: photosphere – Sun: surface magnetism

Online-only material: color figures, animations

1. INTRODUCTION

The properties of small-scale magnetic features on the solar photosphere have been studied for many years (e.g., Harvey & Martin 1973; Wang et al. 1995; Hagenaar et al. 2008; de Wijn et al. 2008). Such features are continually evolving due to interactions with one another (Schrijver et al. 1997; Parnell 2001; Thornton & Parnell 2011; Iida et al. 2012) and the influence of underlying photospheric flows (Leighton et al. 1962; Rieutord et al. 2008; Rieutord & Rincon 2010).

Theoretical studies have shown that most connections between small-scale magnetic features close low down in the corona and that a single feature may be connected to many tens of other features at any time (Schrijver & Title 2002; Priest et al. 2002; Close et al. 2003, 2004). The complex evolution of these magnetic features on the photosphere may significantly heat the low corona through braiding and reconnection of the magnetic fields connecting them (e.g., Parnell & Galsgaard 2004; Berger & Asgari-Targhi 2009; Pontin et al. 2011).

Previous studies of the small-scale coronal field, using either observed or synthetic magnetograms as the lower-boundary condition, include those of van Ballegoijen et al. (1998), Schrijver & Title (2002), Close et al. (2003), Close et al. (2004), Longcope & Parnell (2009), and Cranmer & van Ballegoijen (2010). A limitation of the above studies is that they consider only potential magnetic fields and independent extrapolations of the coronal field for each magnetogram. In contrast, the simulations in this Letter produce a continuous evolution of a non-linear, force-free (nlff) coronal field, driven by a time series of observed magnetograms. An nlff field is a step up in complexity from a potential field as it allows for the existence of electric currents and free magnetic energy. In addition, the continuous nature of this technique means that the evolution of the magnetic field is smooth and current systems are maintained from one step to the next. This technique has been successfully applied in a previous study (Meyer et al. 2013, hereafter Paper I),

in which the coronal field was simulated from a series of synthetic magnetograms (Meyer et al. 2011). Here, we show that the same technique may also be directly applied to observed magnetogram data.

In this Letter, we mainly focus on the build-up, storage, and dissipation of magnetic energy in the coronal field simulations. We discuss both the volume-integrated free magnetic energy and energy dissipated, as well as the spatial location of these two quantities. Finally, we compare the spatial location of energy dissipation within our model to coronal images observed at the same time as the magnetograms. The Letter is outlined as follows. In Section 2 the observations and coronal model are discussed. Results are given in Section 3 and a discussion in Section 4.

2. OBSERVATIONS AND MODEL

2.1. *SDO*/HMI Data

A series of 1919 *Solar Dynamics Observatory* (*SDO*)/Helioseismic and Magnetic Imager (HMI; Scherrer et al. 2012) magnetograms of 45 s cadence is considered for this study, running from 00:00 to 23:59 UT on 2011 January 18. Two data sets are extracted from the full disk images, of size $129'' \times 129''$ (93.6×93.6 Mm, data set 1), with bottom left corner at $(-463''.4, -68''.6)$; and $64''.5 \times 64''.5$ (46.8×46.8 Mm, data set 2) with bottom left corner at $(-507''.2, -27''.2)$. The regions are tracked and de-rotated, then smoothed temporally to remove five minute oscillations, by averaging over nine magnetograms.

Using the technique of Thornton & Parnell (2011), the noise in the data is estimated to be $\sigma = 4.43$ G. We set every pixel of absolute value less than 2σ equal to zero, reducing the average mean field of data set 1 from 5.02 G to 2.46 G, and data set 2 from 7.23 to 4.72 G. Figure 1(a) shows a graph of the mean field as a function of time, after correction, for data sets 1 (gray) and 2 (black). Although the value of the mean field has been significantly reduced in each case, the general

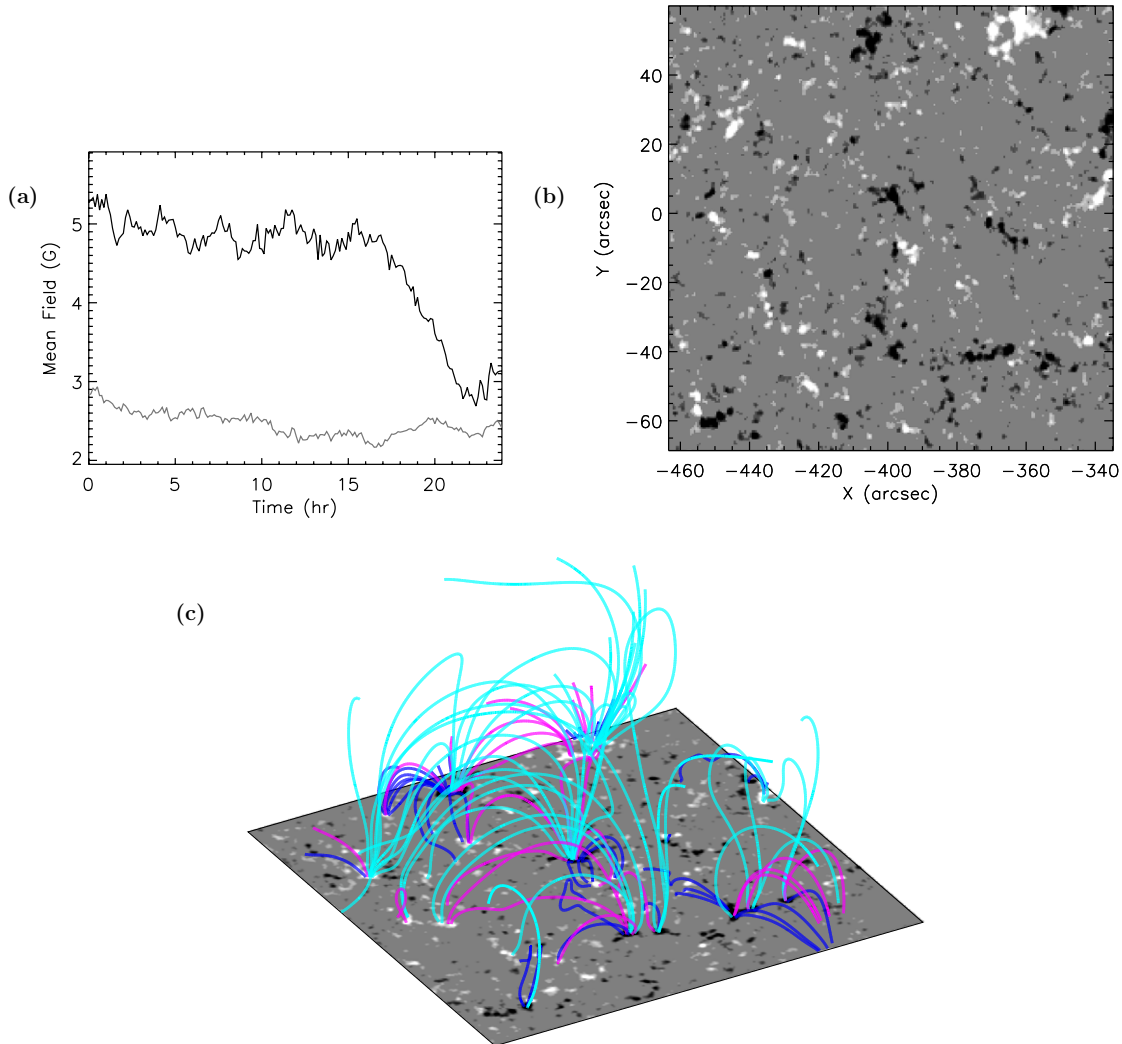


Figure 1. (a) Mean magnetic field for data sets 1 (gray) and 2 (black). (b) Magnetogram from data set 1 at $t = 0$ hr, after correction, saturated at ± 30 G. (c) Coronal magnetic field image shown at $t = 3.12$ hr for simulation 1. The magnetogram is saturated at ± 30 G. Selected coronal field lines are shown, reaching maximum heights of < 7.5 Mm (dark blue), $7.5\text{--}15$ Mm (magenta), and > 15 Mm (pale blue).

(Animations (movie 1, movie 2, and movie 3) and a color version of this figure are available in the online journal.)

shape of the curves remains the same. Also, through considering the magnetograms before and after noise subtraction, the main magnetic features are maintained, therefore the overall behavior of the regions is preserved. (See movie 1, which shows data set 1 before (left) and after (right) all corrections have been applied.) The main effect of the correction is to remove small-scale, short-term variations and emphasize the larger flux concentrations. This is necessary so that the magnetograms may be applied directly as a lower-boundary condition in the time-dependent numerical simulations.

For the three-dimensional simulations, the magnetograms are required to be in complete flux balance, so we also correct them for imbalance using same technique as Mackay et al. (2011). Data set 1 is already roughly in flux balance; the mean imbalance is 2.3% and the imbalance per pixel is at most 3 G, so is comparable to the noise level. The correction reduces the mean field by less than 0.002 G. Data set 2 requires more correction, as it has an average imbalance of 23%. Here, correction further reduces the mean field to 4.51 G.

Finally, the magnetograms are rebinned to double their resolution, as this reduces numerical dissipation in the

coronal model. This results in a 512×512 pixel region, and a 256×256 pixel region, each with pixel size 0.183 Mm. Figure 1(b) shows the first magnetogram in data set 1, after correction.

2.2. Coronal Model

The prepared HMI magnetogram series are used directly as a lower-boundary condition to drive the evolution of the coronal magnetic field. For the full three-dimensional model, we choose numerical boxes composed of $512 \times 512 \times 256$ grid cells ($93.6 \times 93.6 \times 46.8$ Mm³) for data set 1 (hereafter simulation 1), and $256 \times 256 \times 200$ grid cells ($46.8 \times 46.8 \times 36.6$ Mm³) for data set 2 (hereafter simulation 2). In each case, the box is periodic in the x - and y -directions and closed at the top. The initial condition for each model is a potential field extrapolated from the first magnetogram. We use a technique known as the magnetofrictional method (Yang et al. 1986) to evolve the coronal field through a continuous series of quasi-static, nlff states (e.g., van Ballegoijen et al. 2000; Mackay et al. 2011; Meyer et al. 2013). The magnetic field, $\mathbf{B} = \nabla \times \mathbf{A}$, is evolved

via the induction equation:

$$\frac{\partial \mathbf{A}}{\partial t} = \mathbf{v} \times \mathbf{B} + \boldsymbol{\epsilon}. \quad (1)$$

The term $\boldsymbol{\epsilon}$ represents hyperdiffusion, which we choose to be of the form

$$\boldsymbol{\epsilon} = \frac{\mathbf{B}}{B^2} \nabla \cdot (\eta_4 B^2 \nabla \alpha), \quad (2)$$

as in van Ballegoijen & Cranmer (2008), where

$$\alpha = \frac{\mathbf{j} \cdot \mathbf{B}}{B^2}. \quad (3)$$

We take $\eta_4 = 1.2 \times 10^6 \text{ km}^4 \text{ s}^{-1}$. Hyperdiffusion smooths gradients in α whilst conserving magnetic helicity. It describes the relaxation of the field toward a state of constant α (Boozer 1986; Bhattacharjee & Hameiri 1986; Strauss 1988), although, due to constant stressing of the field by lower-boundary motions, such a state is never reached.

The magnetofrictional velocity is proportional to the Lorentz force and is determined as

$$\mathbf{v} = \frac{1}{\nu} \frac{\mathbf{j} \times \mathbf{B}}{B^2}, \quad (4)$$

where ν is the coefficient of friction, with $\nu^{-1} = 3.7 \times 10^4 \text{ km}^2 \text{ s}^{-1}$. This term evolves the coronal field toward a state where $\mathbf{j} \times \mathbf{B} = 0$. Following van Ballegoijen et al. (2000), ν is chosen to be sufficiently small that the coronal field quickly adjusts to photospheric boundary motions, ensuring that $\mathbf{j} \times \mathbf{B}$ remains small everywhere. A typical length scale in the photosphere is the radius of a supergranule ($\approx 13,000 \text{ km}$; Hirzberger et al. 2008) and a typical velocity is $0.5\text{--}1 \text{ km s}^{-1}$ (Parnell 2001), giving a timescale of $3.8\text{--}7.5 \text{ hr}$ for a magnetic feature to travel from supergranule center to edge. A typical relaxation velocity within the corona in our model is 25 km s^{-1} . Considering a relatively large coronal loop within the model, we assume it to be semicircular and to connect magnetic features across the width of a supergranule ($\approx 26,000 \text{ km}$), giving it a length of $\approx 41,000 \text{ km}$. The relaxation time along the loop at 25 km s^{-1} is 27 minutes, 8–16 times faster than the photospheric timescale given. It should be noted that within each simulation, the normal magnetic field component at the photosphere exactly reproduces the observations from SDO/HMI at each 45 s time interval, corresponding to the observation time of the magnetograms. (See movie 2, which shows the observed magnetic field (left) and model photosphere (right) from simulation 1.)

3. RESULTS

Figure 1(c) shows an image from simulation 1 with a selection of coronal magnetic field lines plotted. Similarly, movie 3 shows a 5 hr time series of this figure, and illustrates the connectivity and evolution of the coronal magnetic field.

As in Paper I, the time evolution of free magnetic energy within our model is considered. This is defined as

$$E_f(t) = \int_V \frac{B_{\text{nl}}^2 - B_{\text{p}}^2}{8\pi} dV, \quad (5)$$

where \mathbf{B}_{nl} is the nlff magnetic field and \mathbf{B}_{p} is the corresponding potential magnetic field. Figure 2(a) shows a plot of free magnetic energy as a function of time for simulations 1

(gray) and 2 (black). The mean free energy is $3.1 \times 10^{27} \text{ erg}$ ($7 \times 10^{-3} \text{ erg cm}^{-3}$) and $1.1 \times 10^{27} \text{ erg}$ ($13 \times 10^{-3} \text{ erg cm}^{-3}$) for simulations 1 and 2. These are comparable to the value of $18 \times 10^{-3} \text{ erg cm}^{-3}$ found for the synthetic magnetograms in Paper I. At any one time, there is more than enough free magnetic energy available to explain small-scale impulsive events such as nanoflares ($\approx 10^{24} \text{ erg}$; Parker 1988).

To determine where free magnetic energy is stored within the field, we consider the free magnetic energy density, $(B_{\text{nl}}^2 - B_{\text{p}}^2)/8\pi$, integrated in z :

$$E_f(x, y) = A \int_{z_{\text{min}}}^{z_{\text{max}}} \frac{B_{\text{nl}}^2(x, y, z) - B_{\text{p}}^2(x, y, z)}{8\pi} dz, \quad (6)$$

where $z_{\text{min}} = 0 \text{ Mm}$, $z_{\text{max}} = 46.8 \text{ Mm}$, and $A = (0.183 \text{ Mm})^2$ is the xy area of a pixel. Figure 3(a) shows this quantity for simulation 1, where white patches indicate areas where the free energy density is positive ($\mathbf{B}_{\text{nl}} > \mathbf{B}_{\text{p}}$) and black patches where it is negative ($\mathbf{B}_{\text{nl}} < \mathbf{B}_{\text{p}}$). Note that the total volume-integrated free magnetic energy is always positive (Figure 2(a)). Contours of B_z at $z = 0 \text{ Mm}$ are overlaid in blue (positive) and green (negative). As in Paper I, we define the free magnetic energy to be “stored” at locations where the line-of-sight (LOS) integrated free energy density is positive. The free magnetic energy appears to be mainly stored in large patches between many magnetic features, as can be seen in Figure 3(a) and movie 4. The movie shows that many of these patches are long-lived, lasting several hours. Figure 2(b) shows the free magnetic energy (integrated in x and y) as a function of height, for simulation 1. This is calculated as

$$E_f(z) = L_z \int_{y_{\text{min}}}^{y_{\text{max}}} \int_{x_{\text{min}}}^{x_{\text{max}}} \frac{B_{\text{nl}}^2(x, y, z) - B_{\text{p}}^2(x, y, z)}{8\pi} dx dy, \quad (7)$$

where $x_{\text{min}} = y_{\text{min}} = 0 \text{ Mm}$, $x_{\text{max}} = y_{\text{max}} = 93.6 \text{ Mm}$, and $L_z = 0.183 \text{ Mm}$ is the pixel size in z . The bulk of the free energy is stored below 10 Mm , with peaks around 1 Mm . This is in agreement with Paper I, where it was found that most of the free energy is stored along low-lying, twisted connections between magnetic features.

We also consider the energy that is continually dissipated within the simulations due to the relaxation processes (see Paper I for a full description). This is defined as

$$Q = \frac{B^2}{4\pi} (\nu |\mathbf{v}|^2 + \eta_4 |\nabla \alpha|^2). \quad (8)$$

Here, values of ν and η_4 are chosen for numerical reasons. On the real Sun, the magnetic carpet is likely to develop structures on a wide range of spatial scales, including scales much smaller than those simulated here. Transport of magnetic energy to such scales is likely to occur via a turbulent cascade, that is independent of the details of the energy dissipation process. For this reason, we expect the energy dissipation rate in our model to be independent of the values of ν and η_4 . This assumption will be further tested in future, higher resolution simulations. Figure 2(c) shows the rate of energy dissipation as a function of time, for simulations 1 (gray) and 2 (black). The mean value for simulation 1 is $5.4 \times 10^4 \text{ erg cm}^{-2} \text{ s}^{-1}$, which is composed of a contribution of $5 \times 10^4 \text{ erg cm}^{-2} \text{ s}^{-1}$ (93%) due to friction and $4 \times 10^3 \text{ erg cm}^{-2} \text{ s}^{-1}$ due to hyperdiffusion. This is slightly lower than the estimated values for quiet-Sun coronal radiative losses ($10^5 \text{ erg cm}^{-2} \text{ s}^{-1}$,

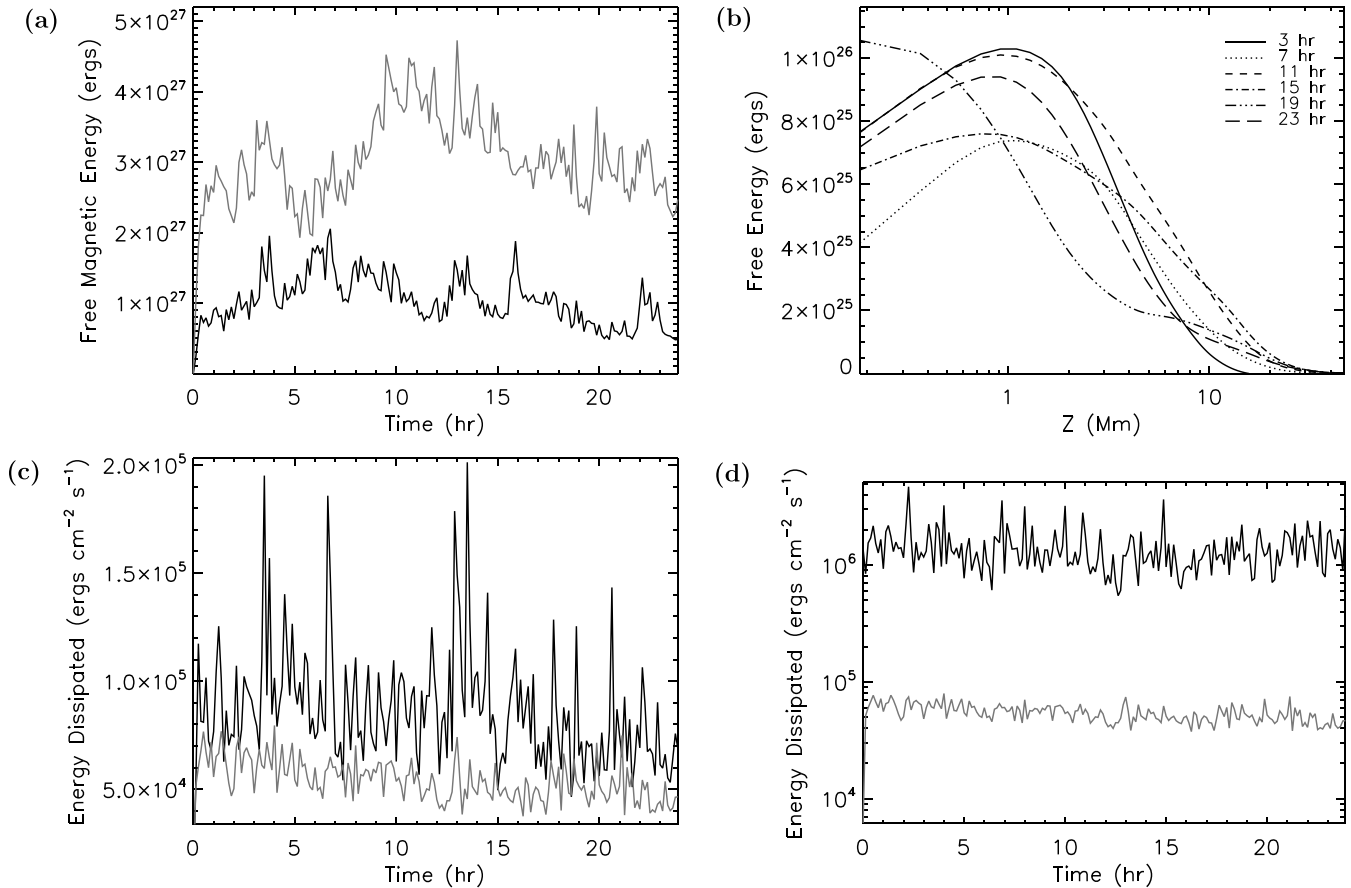


Figure 2. (a) Free magnetic energy as a function of time for simulations 1 (gray) and 2 (black). (b) Free magnetic energy as a function of height for simulation 1. (c) Rate of energy dissipation per unit area as a function of time, for simulations 1 (gray) and 2 (black). (d) Mean (gray) and maximum (black) energy dissipation as a function of time for simulation 1.

Withbroe & Noyes 1977; and $4.9 \times 10^5 \text{ erg cm}^{-2} \text{ s}^{-1}$, Habbal & Grace 1991). However, Equation (8) indicates that Q is dependent upon magnetic field strength. Simulation 2, which has a higher mean field of 4.5 G after noise removal, has a mean energy dissipation of $8.7 \times 10^4 \text{ erg cm}^{-2} \text{ s}^{-1}$ ($8 \times 10^4 \text{ erg cm}^{-2} \text{ s}^{-1}$ due to friction, $7 \times 10^3 \text{ erg cm}^{-2} \text{ s}^{-1}$ due to hyperdiffusion), with peak values of up to $2 \times 10^5 \text{ erg cm}^{-2} \text{ s}^{-1}$. Four separate simulations were run in Paper I, each with the same time-evolving photospheric boundary condition (mean field 4.8 G). In three of the simulations, a uniform overlying coronal magnetic field was included in the x -direction. The fourth simulation had no overlying field. The simulations discussed in this Letter include no overlying field, so we compare these to the no overlying field simulation of Paper I. It is found that the rate of energy dissipation in simulation 2 in this study is almost three times larger than that of Paper I ($8.7 \times 10^4 \text{ erg cm}^{-2} \text{ s}^{-1}$ compared to $3.1 \times 10^4 \text{ erg cm}^{-2} \text{ s}^{-1}$). These values are different due to differences between the observed and synthetic magnetograms. One such difference is that magnetic features in the synthetic magnetograms are more “spread out,” resulting in lower peaks in $|B_z|$ at the photosphere. An improvement to the synthetic magnetograms would be to have narrower features with greater peak $|B_z|$. This will be considered in a future study.

Although the mean energy dissipation for each simulation was found to be lower than the expected values for coronal radiative losses, localized regions yield much higher values. Figure 2(d) shows a graph of the mean (gray) and maximum (black) energy dissipation as a function of time for simulation 1.

It can be seen that the maximum energy dissipation is an order of magnitude greater than the mean value. We find an average peak of $1.4 \times 10^6 \text{ erg cm}^{-2} \text{ s}^{-1}$ for simulation 1 and $1.8 \times 10^6 \text{ erg cm}^{-2} \text{ s}^{-1}$ for simulation 2. This is in line with the observed values of quiet-Sun coronal radiative losses. It should also be pointed out that the mean field of both data sets was significantly reduced due to noise removal. Therefore, if higher resolution and lower noise magnetograms are applied (e.g., SUNRISE; Solanki et al. 2010; Barthol et al. 2011) with a higher mean field strength, then a larger dissipation is expected. The values presented here should be considered as a lower bound. It should, however, be noted that the energy dissipation is treated in a simplified manner and we do not presently follow the corresponding plasma processes.

Another quantity of interest is the spatial location of the energy dissipation within the simulation. Similarly to the free energy density, we integrate Q in z ,

$$E_q(x, y) = \int_{z_{\min}}^{z_{\max}} Q(x, y, z) dz, \quad (9)$$

and consider its location in the xy -plane. An example from simulation 1 is shown in Figure 3(b). The image is saturated at $2 \times 10^5 \text{ erg cm}^{-2} \text{ s}^{-1}$ and it can be seen that many locations exhibit energy dissipation above this level. As was found in Paper I, the evolution of the LOS integrated Q is much more rapid and “bursty” than the free energy (see movie 5). In addition, the energy dissipation is greatest low down, near the evolving magnetic features, and rapidly drops off with

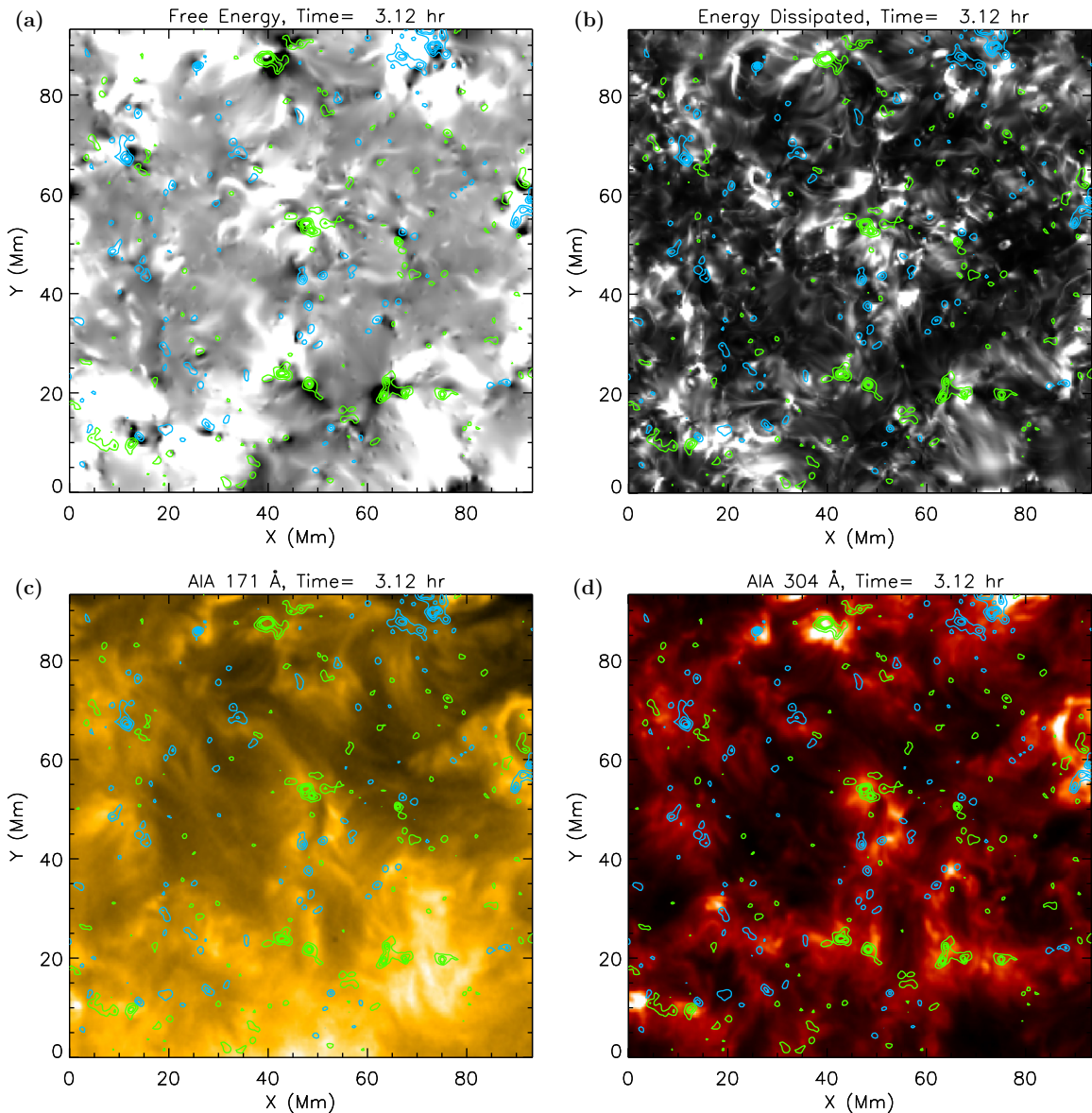


Figure 3. (a) Free magnetic energy density, integrated in z and viewed in the xy -plane, saturated at $\pm 2.3 \times 10^{22}$ erg. White (black) indicates positive (negative) free energy density. (b) Rate of energy dissipation, Q , integrated in z and viewed in the xy -plane, saturated at 2×10^5 erg $\text{cm}^{-2} \text{s}^{-1}$. (c) AIA 171 Å intensity image. (d) AIA 304 Å intensity image. All images are for simulation 1, with positive (blue) and negative (green) contours of B_z at $z = 0$ Mm overplotted at levels of $\pm[15, 45, 75, 105]$ G.

(Animations (movie 4 and movie 5) and a color version of this figure are available in the online journal.)

increasing height. The xy -plane images of energy dissipation are compared to SDO/Atmospheric Imaging Assembly (AIA) 171 Å and 304 Å images taken at the same time as the magnetograms. AIA 304 Å shows chromospheric and transition region plasma with a characteristic temperature of 50,000 K, while AIA 171 Å shows the quiet corona and upper transition region, at a characteristic temperature of 630,000 K (Lemen et al. 2012). Figures 3(c) and (d) show example AIA 171 Å and AIA 304 Å intensity images at the same time as image (b) for comparison. The regions of increased energy dissipation are not an exact match to the brightenings seen in AIA, but some specific events and features do appear to coincide. In general, dark patches in the energy dissipation images are roughly co-located with darker regions in AIA. Movie 5 shows the LOS integrated energy dissipation (left) with AIA 304 Å images (right). It should be noted that the present simulations

consider only a small area and apply periodic boundary conditions, therefore an exact match cannot be expected. This may affect the exact levels of energy storage and dissipation. In the future, we will consider a larger area for simulation that is centered on small-scale events observed in the AIA coronal images, to see whether there is any correlation between the events and regions of increased energy dissipation.

4. DISCUSSION

In this Letter, we have simulated the small-scale coronal field deduced from a set of SDO/HMI magnetograms to consider the build-up, storage, and dissipation of magnetic energy. The coronal modeling technique is driven by photospheric boundary motions, which exactly reproduce the HMI observations, to continuously evolve the coronal field through a series of nlff

states. These simulations extend the work of [Paper I](#) by applying the technique to real, observed magnetograms, as opposed to synthetic magnetograms (Meyer et al. 2011).

We find that the amount of free magnetic energy build-up (3.1×10^{27} erg and 1.1×10^{27} erg) is consistent with the results of [Paper I](#), as is the spatial location of free energy storage. The free energy is mainly stored along low-lying connections between many magnetic features. Large regions of positive free energy density are seen to form and may last several hours. The total amount of free energy available at any time is sufficient to explain small-scale, impulsive heating events like nanoflares and X-ray bright points (XBP).

In contrast to [Paper I](#), which used synthetic magnetograms, the rate of energy dissipation is higher and more in line with the values quoted for the radiative losses of the quiet-Sun corona, of 10^5 erg cm⁻² s⁻¹ (Withbroe & Noyes 1977) and 4.9×10^5 erg cm⁻² s⁻¹ (Habbal & Grace 1991). The highest rates of energy dissipation are found for simulation 2, with a mean of 8.7×10^4 erg cm⁻² s⁻¹ and peaks of on average 1.8×10^6 erg cm⁻² s⁻¹. This region produced higher dissipation than simulation 1 as it had a higher mean field strength. It should be noted that in the process of removing noise from the magnetograms so that they may be successfully used as an evolving lower-boundary condition, the mean field for both data sets was significantly reduced. Therefore, the energy dissipation calculated here may be regarded as a lower bound. Additional studies will consider this in the future.

Images of energy dissipation were compared to AIA 171 Å and 304 Å coronal images from the same time. While regions of increased energy dissipation do not exactly match the brightenings observed in AIA, in general brighter (darker) regions in the energy dissipation images do appear to be roughly co-located with brighter (darker) regions in the AIA images.

In this study, the regions considered are small, and periodic boundaries mean that regions of energy storage and dissipation may be affected by the boundary conditions. A future simulation will consider a larger region, so that a greater central area in the coronal model is unaffected by boundary conditions. Such a simulation may be compared more effectively to coronal images, particularly if the region is chosen so that coronal events of interest, such as XBP, are centered within it.

After successfully using the *SDO*/HMI data, the next stage is to improve upon the coronal model. We plan to extend the model to include pressure and density terms, which will allow us to follow the corresponding plasma processes associated with energy dissipation within our simulations and provide an estimate of the resultant plasma heating.

We thank the anonymous referee for constructive comments, which have improved the Letter. K.A.M. and D.H.M. acknowledge the support of the Leverhulme Trust, STFC, and the EU for their support under FP7. J.S. would like to thank The Royal Society of Edinburgh for their support through the Cormack Vacation Scholarship. We acknowledge the use of *SDO*/HMI and *SDO*/AIA data. Simulations were run using the STFC/SRIF funded UKMHD cluster.

REFERENCES

- Barthol, P., Gandorfer, A., Solanki, S. K., et al. 2011, *SoPh*, **268**, 1
- Berger, M. A., & Asgari-Targhi, M. 2009, *ApJ*, **705**, 347
- Bhattacharjee, A., & Hameiri, E. 1986, *PhRvL*, **57**, 206
- Boozar, A. H. 1986, *JPIPh*, **35**, 133
- Close, R. M., Parnell, C. E., Longcope, D. W., & Priest, E. R. 2004, *ApJL*, **612**, L81
- Close, R. M., Parnell, C. E., Mackay, D. H., & Priest, E. R. 2003, *SoPh*, **212**, 251
- Cranmer, S. R., & van Ballegooijen, A. A. 2010, *ApJ*, **720**, 824
- de Wijn, A. G., Lites, B. W., Berger, T. E., et al. 2008, *ApJ*, **684**, 1469
- Habbal, S. R., & Grace, E. 1991, *ApJ*, **382**, 667
- Hagenaar, H. J., DeRosa, M. L., & Schrijver, C. J. 2008, *ApJ*, **678**, 541
- Harvey, K. L., & Martin, S. F. 1973, *SoPh*, **32**, 389
- Hirzberger, J., Gizon, L., Solanki, S. K., & Duvall, T. L. 2008, *SoPh*, **251**, 417
- Iida, Y., Hagenaar, H. J., & Yokoyama, T. 2012, *ApJ*, **752**, 149
- Leighton, R. B., Noyes, R. W., & Simon, G. W. 1962, *ApJ*, **135**, 474
- Lemen, J. R., Title, A. M., Akin, D. J., et al. 2012, *SoPh*, **275**, 17
- Longcope, D. W., & Parnell, C. E. 2009, *SoPh*, **254**, 51
- Mackay, D. H., Green, L. M., & van Ballegooijen, A. A. 2011, *ApJ*, **729**, 97
- Meyer, K. A., Mackay, D. H., van Ballegooijen, A. A., & Parnell, C. E. 2011, *SoPh*, **272**, 29
- Meyer, K. A., Mackay, D. H., van Ballegooijen, A. A., & Parnell, C. E. 2013, *SoPh*, **286**, 357
- Parker, E. N. 1988, *ApJ*, **330**, 474
- Parnell, C. E. 2001, *SoPh*, **200**, 23
- Parnell, C. E., & Galsgaard, K. 2004, *A&A*, **428**, 595
- Pontin, D. I., Wilmot-Smith, A. L., Hornig, G., & Galsgaard, K. 2011, *A&A*, **525**, A57
- Priest, E. R., Heyvaerts, J. F., & Title, A. M. 2002, *ApJ*, **576**, 533
- Rieutord, M., Meunier, N., Roudier, T., et al. 2008, *ApJL*, **479**, L17
- Rieutord, M., & Rincon, F. 2010, *LRSP*, **7**, 2
- Scherrer, P. H., Schou, J., Bush, R. I., et al. 2012, *SoPh*, **275**, 207
- Schrijver, C. J., & Title, A. M. 2002, *SoPh*, **207**, 223
- Schrijver, C. J., Title, A. M., van Ballegooijen, A. A., Hagenaar, H. J., & Shine, R. A. 1997, *ApJ*, **487**, 424
- Solanki, S. K., Barthol, P., Danilovic, S., et al. 2010, *ApJL*, **723**, L127
- Strauss, H. R. 1988, *ApJ*, **326**, 412
- Thornton, L. M., & Parnell, C. E. 2011, *SoPh*, **269**, 13
- van Ballegooijen, A. A., & Cranmer, S. R. 2008, *ApJ*, **682**, 644
- van Ballegooijen, A. A., Nisenson, P., Noyes, R. W., et al. 1998, *ApJ*, **509**, 435
- van Ballegooijen, A. A., Priest, E. R., & Mackay, D. H. 2000, *ApJ*, **539**, 983
- Wang, J., Wang, H., Tang, F., Lee, J. W., & Zirin, H. 1995, *SoPh*, **160**, 277
- Withbroe, G. L., & Noyes, R. W. 1977, *ARA&A*, **15**, 363
- Yang, W. H., Sturrock, P. A., & Antiochos, S. K. 1986, *ApJ*, **309**, 383